

Perturbation growth in terms of barotropic alignment properties

By G. RIVIÈRE¹*, B. L. HUA² and P. KLEIN²

¹*Laboratoire de Météorologie Dynamique, Paris, France*

²*Laboratoire de Physique des Océans, Plouzanne, France*

(Received 24 April 2002; revised 15 November 2002)

SUMMARY

In order to study the error growth due to initial uncertainties in the model state, this paper examines the alignment dynamics of the perturbation velocity vector in quasi-geostrophic flows. In a barotropic context, the time evolution of the perturbation velocity field is the sum of two terms: (i) the stretching of the perturbation velocity vector by the basic-state velocity-gradient tensor (denoted $\nabla \mathbf{u}$) and (ii) the perturbation ageostrophic pressure gradient, which also depends on $\nabla \mathbf{u}$. Different analytical results show that such a system has two types of preferred orientation that induce kinetic-energy growth: one orientation concerns one eigenvector of $\nabla \mathbf{u}$, the other one is linked to a fixed point of the orientation equation of the perturbation velocity vector written in strain coordinates. This analytical diagnostic is confirmed by using Monte-Carlo techniques in a quasi-geostrophic oceanic-basin model of a stratified wind-driven double-gyre circulation, and these orientations are shown to be the most probable. These preferred orientations are of great importance for diagnosing the most probable kinetic-energy generation rate at each grid point. An interesting outcome is that the kinetic-energy error field is localized in regions where the norm of $\nabla \mathbf{u}$ is large.

KEYWORDS: Alignment dynamics Kinetic-energy growth Local instability

1. INTRODUCTION

Even though conventional parallel-flow problems have proved useful in understanding the barotropic and baroclinic instability mechanisms involved in large-scale atmospheric and oceanic flows, actual flows are non-parallel and zonally varying. Many phenomena, thus, tend to occur in preferred regions such as, for instance, the specific localization of cyclone emergence in midlatitudes. Understanding regional cyclogenesis is of great importance because the spatial distribution of the synoptic eddy fluxes determine the position of the storm tracks, which themselves influence the planetary-wave behaviour and the atmospheric low-frequency variability (Simmons *et al.* 1983; Hoskins *et al.* 1983). Frederiksen (1983) characterized the local stability properties of stationary zonally varying flows by looking at the geographical distribution of the unstable normal modes of the linear eigenvalue problem, and found good correspondences with observations. However, he could not explain the physical mechanism involved in the localization.

Pierrehumbert (1984) has applied the WKB method to this problem, by separating global modes and local modes that are localized at the point of maximum shear, but such an approach needs a scale separation between the basic flow and the perturbation. By completing a systematic study of the equations for linearized energetics, Mak and Cai (1989) (referred to as MC in the following) in a barotropic case, and Cai and Mak (1990) in a baroclinic situation, have generalized the well known parallel-flow result that ‘a perturbation extracts energy if its structure leans against the shear’. In a barotropic context, their generalization states that in order ‘to optimally extract kinetic energy from the basic flow, a perturbation must be elongated locally along the axis of contraction of the basic deformation field. If the perturbation is oriented locally along the axis of dilatation, it will lose kinetic energy to the basic flow’. In parallel-flow problems, for the category of ‘unstable wave numbers’, an equilibrated structure exists that corresponds to

* Corresponding author: Laboratoire de Météorologie Dynamique, ENS, 24 rue Lhomond, 75005 Paris, France.
e-mail: griviere@lmd.ens.fr

© Royal Meteorological Society, 2003.

the unstable normal mode, with a specific orientation of the perturbation structure with respect to the shear.

Thus, building upon the generalization proposed by MC, the following question emerges naturally: is there a generalization for localized instability problems of the property of the unstable normal modes of parallel-flow problems that favours specific orientations of growing perturbations? More specifically, can one analytically predict which orientations will favour perturbation energy growth, and in which regions will these locally equilibrated structures emerge? These questions are directly related to cyclogenesis problems: for instance, Kucharski and Thorpe (2001) showed that barotropic growth can dominate the initial phase of a cyclonic development, and that specific horizontal perturbation structures are needed within specific regions to lead to strong and fast cyclonic development. A related issue concerns predictability problems: if the most probable structure of growing perturbations can be determined analytically, then the average rate of energy extraction from the basic flow by the perturbations can be forecast, and this is an important diagnostic for characterizing the limit of predictability of a given flow.

In the present paper, we attempt to answer this question by considering the linearized momentum equations, as examined by MC but in their Lagrangian barotropic quasi-geostrophic form without taking friction into account.

The essential idea (cf. Straub 2003) is that, if the perturbation ageostrophic pressure gradient were negligible, a closed system would appear for the perturbation velocity vector, in which the time evolution would be simply determined through its stretching by the basic-state shear $\nabla \bar{\mathbf{u}}$.

This important observation, supplemented by an analytical approximation of the pressure-gradient term, leads us to rationalize some features of the localized instability problem for a quasi-geostrophic model, namely (i) the tendency for alignment of the perturbation velocities with predictable directions of the basic-state flow, (ii) the spatial localization of its generation rates and (iii) the regionalization of the error fields.

Moreover, we use results for alignment properties which have been established recently for the growth of tracer gradients in two-dimensional turbulence (Lapeyre *et al.* (1999), referred to as L99 hereafter); these results also address the problem of the stretching of a vector field by the velocity-gradient tensor $\nabla \bar{\mathbf{u}}$. Our approach for numerical diagnostics of perturbation growth differs from the studies of localized instability cited above, and relies instead on a Monte-Carlo approach whereby an ensemble of simulations, initialized with small random perturbations of a reference flow, is allowed to evolve for a length of time that corresponds to about five to ten straining timescales of the basic state. Statistical properties of the perturbations that have emerged after that finite time are then diagnosed for specific diagnostics.

The present paper is organized as follows: section 2 discusses the linearized momentum equations and their comparison with the equations for the growth of tracer gradients; section 3 reports on numerical diagnostics concerning alignment dynamics, generation rates and error fields; and section 4 provides a discussion of our results.

2. BAROTROPIC PERTURBATION EQUATIONS

(a) *Time evolution of the perturbation velocity*

To study the kinetic-energy error growth, we have to consider the linearized equations for the perturbation velocity field. The ageostrophic momentum equations for the basic state are written here for simplicity in their barotropic form and without the

β -effect (the β -effect is considered later).

$$\frac{\overline{D}\overline{\mathbf{u}}}{Dt} = -\nabla\overline{p}_1, \quad (1)$$

where $\overline{D}/Dt = \partial/\partial t + (\overline{\mathbf{u}} \cdot \nabla)$ denotes the geostrophic total derivative, $\overline{\mathbf{u}}$ is the basic-state geostrophic velocity field and \overline{p}_1 the ageostrophic pressure field. The momentum equations of the linearized perturbation system can be written as

$$\frac{\overline{D}\mathbf{u}'}{Dt} = -\nabla\overline{\mathbf{u}} \cdot \mathbf{u}' - \nabla p'_1, \quad (2)$$

where $\nabla\overline{\mathbf{u}}$ is the basic-state velocity-gradient tensor. Bars in (2) denote quantities associated with the reference flow, while primes denote perturbations. By taking the curl of (2) we obtain the linearized perturbation vorticity equation

$$\frac{\overline{D}\omega'}{Dt} = -\mathbf{u}' \cdot \nabla\overline{\omega}. \quad (3)$$

$\omega \equiv \partial_x v - \partial_y u$ (where $\partial_x = \partial/\partial x$ and $\partial_y = \partial/\partial y$) denotes the vertical component of relative vorticity. In order to localize the kinetic-energy error growth, let us now consider the local kinetic energy equation derived from (2)

$$\frac{1}{2} \frac{\partial u'^2}{\partial t} = -\overline{\mathbf{u}} \cdot \nabla \left(\frac{u'^2}{2} \right) - \mathbf{u}' \cdot (\nabla\overline{\mathbf{u}} \cdot \mathbf{u}') - \mathbf{u}' \cdot \nabla p'_1. \quad (4)$$

The physical interpretation of the three terms of the right-hand side of (4) have been developed by MC. The second term is the generation rate of the local perturbation energy, whereas the two other ones (advection of the energy by the basic flow and the pressure work) redistribute the perturbation energy spatially and do not contribute to the global energetics. The generation rate can be viewed as the scalar product of two vectors \mathbf{E} and \mathbf{D} as defined by MC

$$\begin{aligned} \mathbf{E} &= \left\{ \frac{1}{2}(v'^2 - u'^2), -u'v' \right\}, \\ \mathbf{D} &= (\partial_x \overline{u} - \partial_y \overline{v}, \partial_x \overline{v} + \partial_y \overline{u}). \end{aligned} \quad (5)$$

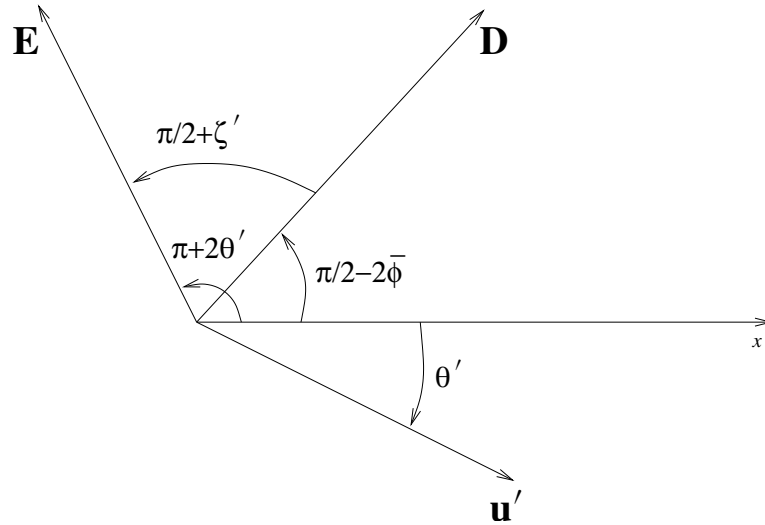
\mathbf{E} depends on the perturbation structure and \mathbf{D} represents the basic-state deformation field where $\overline{\sigma}_n \equiv \partial_x \overline{u} - \partial_y \overline{v}$ is the stretching component and $\overline{\sigma}_s \equiv \partial_x \overline{v} + \partial_y \overline{u}$ the shearing component. If $\mathbf{E} \cdot \mathbf{D} > 0$ (or $\mathbf{E} \cdot \mathbf{D} < 0$), the perturbation structure is such that it can extract energy from (or lose energy to) the basic flow. The angle between the two vectors \mathbf{E} and \mathbf{D} is thus essential for determining locally if the perturbation can extract or not energy from the basic flow. As our present study focuses on this angle, let us define different notations that will be useful in the following sections. We decompose the perturbation velocity vector into its modulus $\rho' \equiv |\mathbf{u}'|$ and into its angle θ'

$$\mathbf{u}' = \rho'(\cos \theta', \sin \theta') = \rho' \mathbf{e}', \quad (6)$$

with \mathbf{e}' denoting the unit vector which points in the same direction as \mathbf{u}' .

With this notation, \mathbf{E} can also be decomposed into its modulus (the kinetic energy of the perturbation) and angle

$$\mathbf{E} = \frac{\rho'^2}{2} \{\cos(\pi + 2\theta'), \sin(\pi + 2\theta')\}. \quad (7)$$

Figure 1. Angles defining the directions of the vectors **E** and **D**.

$\bar{\phi}$ is defined as the angle of the principal axes of the basic-state strain-rate tensor

$$(\partial_x \bar{v} + \partial_y \bar{u}, \partial_x \bar{u} - \partial_y \bar{v}) = (\bar{\sigma}_s, \bar{\sigma}_n) = \bar{\sigma}(\cos 2\bar{\phi}, \sin 2\bar{\phi}), \quad (8)$$

where $\bar{\sigma} = |\mathbf{D}| \geq 0$ is the magnitude of the strain rate. With this notation the angle of the vector **D** with the x -axis is $\pi/2 - 2\bar{\phi}$. As shown in Fig. 1, the angle between **E** and **D** is equal to $\pi/2 + \zeta'$ with $\zeta' \equiv 2\theta' + 2\bar{\phi}$. In our notation the fundamental term for the local perturbation growth $\mathbf{E} \cdot \mathbf{D}$ can be expressed as

$$\mathbf{E} \cdot \mathbf{D} = -\mathbf{u}' \cdot (\nabla \bar{\mathbf{u}} \cdot \mathbf{u}') = -\frac{\rho'^2}{2} \bar{\sigma} \sin \zeta', \quad (9)$$

which depends on three terms: the already redistributed kinetic energy $\rho'^2/2 = |\mathbf{u}'|^2/2$, the rate of strain $\bar{\sigma}$, and the angle ζ' , which is studied in section 3(a). Dividing (4) by the kinetic energy $\rho'^2/2$, we obtain the Eulerian exponential kinetic-energy growth rate, and the associated generation term is, thus,

$$\delta \equiv \frac{\mathbf{E} \cdot \mathbf{D}}{\rho'^2/2} = -\bar{\sigma} \sin \zeta',$$

which is hereafter called the exponential kinetic-energy generation rate (using the terminology of MC).

(b) *Influence of $\nabla \bar{\mathbf{u}}$ on the orientation equation of the perturbation velocity*

Let us first consider separately the dynamical influence of $\nabla \bar{\mathbf{u}}$ on the orientation of the perturbation velocity vector, the ageostrophic pressure role is considered in section 2(c). The important point to note is that, if the perturbation ageostrophic pressure gradient is dropped in (2), a closed form is obtained for \mathbf{u}'

$$\frac{D\mathbf{u}'}{Dt} = -\nabla \bar{\mathbf{u}} \cdot \mathbf{u}', \quad (10)$$

i.e. the perturbation velocity field \mathbf{u}' is simply determined through its stretching by the basic-state shear $\nabla \bar{\mathbf{u}}$, which is a known entity. By taking the curl of the approximate equation (10), one can also recover the exact linearized perturbation vorticity equation (3), which is, however, not a closed system for ω' since (3) also depends on \mathbf{u}' . The approximate equation (10) amounts to studying the stretching of a vector field by a given tensor; this approach was first exploited by Straub (2003) to study hydrostatic three-dimensional perturbations in a two-dimensional reference flow. His motivation came from an observation that, in an unstratified and non-rotating limit, (10) for the perturbation velocity is exact and similar in its structure to the tracer-gradient and line-element equations. However, in our quasi-geostrophic model, (10) is only an approximation that permits us to obtain some dynamical information when using the method introduced by L99 for the tracer gradient; this method needs to be adapted to take into account the influence of the ageostrophic pressure-gradient term $\nabla p'_1$ in (2). The exact equation for the tracer gradient is

$$\frac{\overline{D}\nabla\bar{q}}{Dt} = -\nabla\bar{\mathbf{u}}^T\nabla\bar{q}, \quad (11)$$

\bar{q} denoting the tracer field. The difference between (10) and (11) is twofold: (i) for the tracer-gradient evolution, the tensor involved is the transpose of the velocity-gradient tensor and (ii) (11) applies to a gradient vector field while (10) applies to a non-divergent vector field (see section 2(c)). Recent theoretical results on the dynamics of tracer-gradient formation have shown that the tracer-gradient vector aligns with a preferential direction and the gradient magnitude grows exponentially in time. This preferential direction appears naturally when the gradient is decomposed into its norm and angle, as shown by L99. Let us now derive the same equations as those of L99, but for the perturbation velocity. In a quasi-geostrophic context, incompressibility ($\partial_x \bar{u} + \partial_y \bar{v} = 0$) leads to

$$\nabla\bar{\mathbf{u}} = \begin{bmatrix} \partial_x \bar{u} & \partial_y \bar{u} \\ \partial_x \bar{v} & \partial_y \bar{v} \end{bmatrix} = \frac{1}{2} \begin{bmatrix} \bar{\sigma}_n & \bar{\sigma}_s \\ \bar{\sigma}_s & -\bar{\sigma}_n \end{bmatrix} + \frac{1}{2} \begin{bmatrix} 0 & -\bar{\omega} \\ \bar{\omega} & 0 \end{bmatrix}. \quad (12)$$

Let us first consider the case of (10) for the velocity perturbation. The projections of (10) on \mathbf{e}' and on $\mathbf{e}'_\perp \equiv (-\sin\theta', \cos\theta')$ lead to two equations, one for the norm ρ' and the other for the angle θ' of the perturbation velocity vector

$$\frac{1}{\rho'^2} \frac{\overline{D}\rho'^2}{Dt} = -\bar{\sigma} \sin(2\theta' + 2\bar{\phi}), \quad (13a)$$

$$2 \frac{\overline{D}\theta'}{Dt} = \bar{\sigma} \{-r_{\text{ow}} - \cos(2\theta' + 2\bar{\phi})\}, \quad (13b)$$

where

$$r_{\text{ow}} \equiv \frac{\bar{\omega}}{\bar{\sigma}}. \quad (14)$$

The dimensionless parameter r_{ow} is the ratio between the vorticity $\bar{\omega}$ and the magnitude of the strain rate $\bar{\sigma}$. The time evolution of ρ' and θ' depends on the relative angle ζ' between the perturbation velocity vector and the axis of contraction of the strain rate. For $|r_{\text{ow}}| < 1$, the eigenvectors of $\nabla\bar{\mathbf{u}}$ correspond to the solutions of the equation $\overline{D}\theta'/Dt = 0$, which leads to the orientations $\zeta' = \zeta'_\pm \equiv \pm \arccos(-r_{\text{ow}})$. The eigenvector of $\nabla\bar{\mathbf{u}}$ with the negative eigenvalue has a stable orientation $\zeta' = \zeta'^{\text{ow}}_-$ leading to kinetic-energy growth, while the eigenvector with the positive eigenvalue has an unstable orientation $\zeta' = \zeta'^{\text{ow}}_+$ leading to kinetic-energy decrease.

A more accurate expression than (13) can be derived in strain coordinates (following L99 and Straub 2003) that only involves ζ'

$$\frac{1}{\rho'^2} \frac{\overline{D}\rho'^2}{Dt} = -\overline{\sigma} \sin \zeta', \quad (15a)$$

$$\frac{\overline{D}\zeta'}{Dt} = \overline{\sigma}(-r' - \cos \zeta'), \quad (15b)$$

where

$$r' \equiv \frac{1}{\overline{\sigma}} \left(\overline{\omega} - 2 \frac{\overline{D}\overline{\phi}}{Dt} \right). \quad (16)$$

The dimensionless parameter r' is the ratio between $\overline{\omega} - 2\overline{D}\overline{\phi}/Dt$ (which is the vorticity minus the rotation of the principal axes of the strain-rate tensor) and the magnitude of the strain rate $\overline{\sigma}$. If $|r'| < 1$, that is for regions where strain dominates, (15b) has two fixed points $\zeta'_{\pm} = \pm \arccos(-r')$, a stable one $\zeta' = \zeta'_-$ and an unstable one $\zeta' = \zeta'_+$. From (15a), the stable orientation ζ'_- corresponds to an exponential growth of the norm ρ' , while the unstable orientation ζ'_+ corresponds to an exponential decay of ρ' . Note that the orientations ζ'_{\pm} have taken into account the rotation rate of \mathbf{D} , which is exactly $-2\overline{D}\overline{\phi}/Dt$.

For the tracer gradient system, we have similar properties, i.e. two fixed points $\zeta_{\pm} \equiv \pm \arccos(r)$ depending on a parameter

$$r \equiv \frac{1}{\overline{\sigma}} \left(\overline{\omega} + 2 \frac{\overline{D}\overline{\phi}}{Dt} \right). \quad (17)$$

We note that $-\overline{\omega}$ in the formulation of the fixed points

$$\zeta'_{\pm} = \pm \arccos \left\{ \frac{1}{\overline{\sigma}} \left(-\overline{\omega} + 2 \frac{\overline{D}\overline{\phi}}{Dt} \right) \right\}$$

is changed into $\overline{\omega}$ in the tracer-gradient formulation

$$\zeta_{\pm} = \pm \arccos(r) = \pm \arccos \left\{ \frac{1}{\overline{\sigma}} \left(\overline{\omega} + 2 \frac{\overline{D}\overline{\phi}}{Dt} \right) \right\}$$

because of the transpose operator in (11). Numerical simulations of two-dimensional turbulence in L99 show that the tracer-gradient orientation is statistically well aligned with the stable direction ζ_- corresponding to tracer-gradient growth. This orientation is significantly more probable than that derived from the stable eigenvector of $\nabla \mathbf{u}^T$ (the Okubo–Weiss criterion—see Okubo (1970) and Weiss (1991)). The difference between the two orientations is that ζ_- takes into account the rotation rate of the strain axes, whereas the eigenvector of $\nabla \mathbf{u}^T$ does not (see L99).

From the perturbation velocity equations, two natural systems emerge. One implies the equivalent Okubo–Weiss criterion and so the preferred orientations are those of the eigenvectors of $\nabla \mathbf{u}$; the other one is analogous to the system of L99 with two preferred orientations $\zeta' = \zeta'_{\pm}$ for a different eigenvalue problem in the strain basis (cf. appendix of L99).

Straub (2003) shows that the condition $|r'| < 1$ exactly implies the centrifugal instability criterion*, whereas the equivalent Okubo–Weiss criterion $|r_{ow}| < 1$ does not

* For which it is known that azimuthal pressure gradient does not influence the instability.

yield the appropriate instability condition. On account of the simple system (15), and of both the numerical simulations of L99 and the recent work of Straub, the expected result (if (10) were exact) would be that ζ' will preferentially align with ζ_-' and not with $\zeta_-^{r_{ow}}$. However, the above inferences suppose that (10) is exact and we show in the next section that the influence of the ageostrophic pressure gradient in (2) is to introduce another term in the orientation equations (13b) and (15b).

(c) *The ageostrophic pressure-gradient influence*

In this section, the complete equation (2) is studied analytically, taking into account both $\nabla \bar{\mathbf{u}}$ and $-\nabla p'_1$ but using a simple approximation of the ageostrophic pressure gradient. As already noted in section 2(a), we are dealing with a stretched vector field \mathbf{u}' that is non-divergent, so that by taking the divergence of (2), we obtain the equation relating the perturbation velocity \mathbf{u}' to the perturbation ageostrophic pressure

$$\Delta p'_1 = 2\{J(\bar{\mathbf{u}}, v') + J(u', \bar{v})\} \quad (18a)$$

$$= 2\{\bar{\sigma}_n \partial_{xy} \psi' - \frac{1}{2}(\bar{\sigma}_s - \bar{\omega}) \partial_x^2 \psi' + \frac{1}{2}(\bar{\sigma}_s + \bar{\omega}) \partial_y^2 \psi'\}, \quad (18b)$$

where J denotes the Jacobian operator, ψ' the perturbation stream function and (u, v) the velocity vector in the Cartesian coordinates (x, y) . To solve for the perturbation ageostrophic pressure p'_1 , we have to invert a Laplacian. Some insight on the local dynamical influence of the pressure perturbation may still be obtained by the following analytical diagnostic that considers a monochromatic perturbation (caveat: even if a monochromatic function is non-local, this approximation is a first step towards diagnosing the pressure-gradient effect)

$$\psi'(x, y) = \text{Re}[A \exp\{i(kx + ly)\}]. \quad (19)$$

This particular perturbation form leads to a new expression of Eq. (18b)

$$\Delta p'_1 = 2\{-\bar{\sigma}_n kl + \frac{1}{2}(\bar{\sigma}_s - \bar{\omega})k^2 - \frac{1}{2}(\bar{\sigma}_s + \bar{\omega})l^2\} \psi'. \quad (20)$$

If we consider $\bar{\sigma}_n$, $\bar{\sigma}_s$ and $\bar{\omega}$ as slowly varying by comparison with the perturbation variations (WKB assumption), the ageostrophic pressure is also monochromatic and its gradient is collinear with the stream function gradient $\nabla \psi'$ and thus perpendicular to the velocity vector \mathbf{u}'

$$-\nabla p'_1 = \frac{2}{k^2 + l^2} \left\{ -\bar{\sigma}_n kl + \frac{1}{2}(\bar{\sigma}_s - \bar{\omega})k^2 - \frac{1}{2}(\bar{\sigma}_s + \bar{\omega})l^2 \right\} \nabla \psi'. \quad (21)$$

With the particular form (19), \mathbf{u}' can be written as

$$\mathbf{u}' = \begin{pmatrix} u' \\ v' \end{pmatrix} = A \sin(kx + ly) \begin{pmatrix} l \\ -k \end{pmatrix}, \quad (22)$$

and the orientation θ' is thus

$$\begin{pmatrix} \cos \theta' \\ \sin \theta' \end{pmatrix} = \pm \begin{pmatrix} \frac{l}{\sqrt{k^2 + l^2}} \\ \frac{-k}{\sqrt{k^2 + l^2}} \end{pmatrix}. \quad (23)$$

This leads to the following calculations

$$-\nabla p'_1 = 2\{\bar{\sigma}_n \cos \theta' \sin \theta' + \frac{1}{2}(\bar{\sigma}_s + \bar{\omega}) \sin^2 \theta' - \frac{1}{2}(\bar{\sigma}_s + \bar{\omega}) \cos^2 \theta'\} \nabla \psi' \quad (24a)$$

$$= (\bar{\sigma}_n \sin 2\theta' - \bar{\sigma}_s \cos 2\theta' - \bar{\omega}) \nabla \psi' \quad (24b)$$

$$= \bar{\sigma}(r_{ow} + \cos \zeta') \rho' \mathbf{e}'_{\perp}. \quad (24c)$$

As the pressure gradient aligns with \mathbf{e}'_{\perp} , the local spatial influence of $\nabla p'_1$ is simply to modify the orientation equations (13b) or (15b) and not the norm equations (13a) or (15a). Let us denote $P_{\theta}(p'_1) \equiv -\nabla p'_1 \cdot \mathbf{e}'_{\perp} / \rho'$, the additional term on the orientation equation due to the ageostrophic pressure gradient; in a monochromatic context, we obtain the following formula

$$P_{\theta}(p'_1) = \bar{\sigma}(r_{\text{ow}} + \cos \zeta'), \quad (25)$$

which implies a new orientation equation

$$\frac{\overline{D}\theta'}{Dt} = -\frac{1}{2}\bar{\sigma}(r_{\text{ow}} + \cos \zeta') + P_{\theta}(p'_1) = \frac{1}{2}\bar{\sigma}(r_{\text{ow}} + \cos \zeta'). \quad (26)$$

$\overline{D}\theta'/Dt$ is the sum of two terms: the first term on the right-hand side comes from the projection of $-\nabla \bar{\mathbf{u}} \cdot \mathbf{u}'$, the second term is the pressure-gradient component and is twice the opposite value of the first term. The pressure gradient in this equation is, thus, not at all negligible. Both terms are zero if \mathbf{u}' aligns with the eigenvectors of $\nabla \bar{\mathbf{u}}$, and we still have $\overline{D}\theta'/Dt = 0$ for those directions, even in presence of the pressure term. If $\nabla \bar{\mathbf{u}}$ is slowly varying along a Lagrangian path, the eigenvectors directions would, therefore, be the preferred directions for \mathbf{u}' by considering the complete (2). However, the studies of L99 and Straub (2003) have shown the dynamical importance of the variations of $\nabla \bar{\mathbf{u}}$ and, more precisely, of the rotation of the principal axes of the strain-rate tensor. In strain coordinates, the orientation equation in this case is

$$\frac{\overline{D}\zeta'}{Dt} = \bar{\sigma}(r + \cos \zeta'), \quad (27)$$

where $r = (\bar{\omega} + 2\overline{D}\bar{\phi}/Dt)/\bar{\sigma}$ is the parameter defined in (17). The fixed points of (15b), ζ'_{\pm} , are not the fixed points of the complete equation (27). The complete equation (27) has two fixed points determined by $\zeta'_{\pm} \equiv \pm \arccos(-r)$. Our approximation of the pressure term leads us to two couples of preferred directions $(\zeta'^{\text{ow}}_{-}, \zeta'^{\text{ow}}_{+})$ and $(\zeta'^r_{-}, \zeta'^r_{+})$. These two couples seem to be more appropriate to describe the most probable values of ζ' , because the pressure term is known to have a non-negligible influence on the dynamics of \mathbf{u}' . An important point to note is that the productive preferred directions by considering the complete equation (2), ζ'^{ow}_{-} and ζ'^r_{-} , are unstable as shown in appendix A, whereas the productive preferred directions by considering only the simplified system (10), ζ'^{ow}_{-} and ζ'^r_{-} , are stable. The parametrization of the pressure gradient is derived from a strong monochromaticity assumption but, as we see later with the numerical results, the formulation obtained for the projection $P_{\theta}(p'_1)$ of the pressure gradient on the orientation equation is significant.

In appendix B, we verify by taking into account the β -term and by using the same monochromatic perturbation that the β -term does not appear in the orientation equation and, thus, has no influence on the preferred orientations.

To summarize: without the pressure term, two couples of preferred orientations emerge ζ'^{ow}_{\pm} and ζ'^r_{\pm} , with the approximation of the pressure term, another couple emerges ζ'^r_{\pm} . By considering only the productive orientations ζ'^{ow}_{-} , ζ'^r_{-} and ζ'^r_{+} , we can

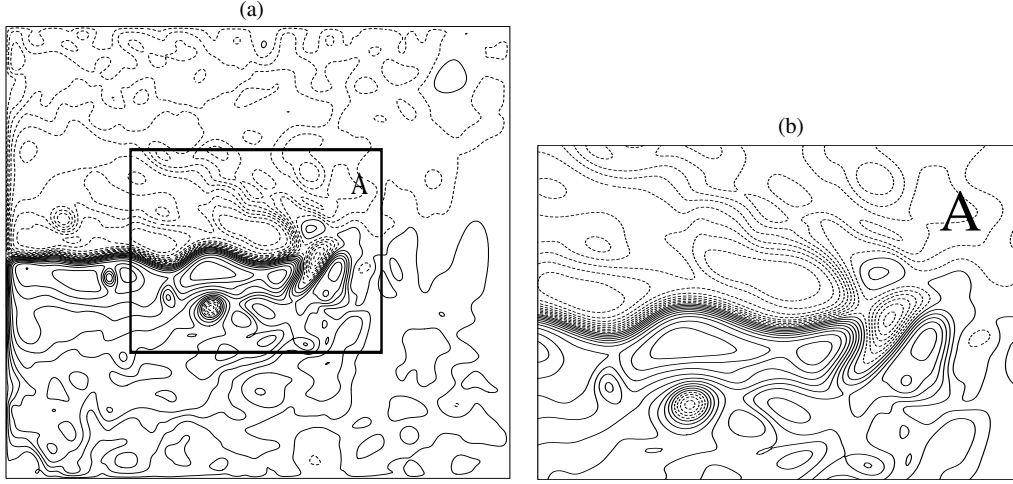


Figure 2. Stream function $\bar{\psi}$ (contour interval $8276 \text{ m}^2\text{s}^{-1}$) of the reference flow ($T = 10$ days) in the first layer; (a) the whole basin, (b) zoom at the end part of the jet: area A.

define three analytical estimates of the exponential generation rate

$$\delta_{\text{ow}} \equiv -\bar{\sigma} \sin(\zeta_{-}^{\text{ow}}) = \sqrt{\bar{\sigma}^2 - \bar{\omega}^2}, \quad |r_{\text{ow}}| < 1, \quad (28a)$$

$$\delta_{r'} \equiv -\bar{\sigma} \sin(\zeta_{-}^{r'}) = \sqrt{\bar{\sigma}^2 - \left(-\bar{\omega} + 2\frac{\bar{D}\bar{\phi}}{Dt}\right)^2}, \quad |r'| < 1, \quad (28b)$$

$$\delta_r \equiv -\bar{\sigma} \sin(\zeta_{-}^r) = \sqrt{\bar{\sigma}^2 - \left(\bar{\omega} + 2\frac{\bar{D}\bar{\phi}}{Dt}\right)^2}, \quad |r| < 1. \quad (28c)$$

We remark that the maximum of δ is equal to $\bar{\sigma}$. It corresponds to the most efficient structure $\zeta' = -\pi/2$, i.e. when \mathbf{u}' is aligned with the axis of contraction of the strain rate and is hereafter denoted as $\delta_{\text{eff}} \equiv \bar{\sigma}$.

3. NUMERICAL RESULTS IN A QUASI-GEOSTROPHIC MODEL

In the present study, results are developed for the classical oceanic case of a wind-driven double gyre using a six-layer quasi-geostrophic model in a rectangular basin. A strong jet separates the southern anticyclonic gyre from the northern cyclonic one. The jet has meanders which can detach and form eddies that travel westward. An example of the flow is shown in Fig. 2, which represents the stream function $\bar{\psi}$ in the first layer. In the next sections, our study of the localized disturbances and the initial error growth for this control flow will focus on the limited area A located at the exit of the jet (Fig. 2(b)) because of its more turbulent and varied dynamical structures. The numerical model is presented in appendix C.

The results are produced for a particular ensemble of random perturbations. The corresponding Monte-Carlo technique is developed in appendix D. Hereafter, we study perturbation structures that have evolved for ten days (corresponding to roughly five straining timescales of the basic-state flow), from $T = 0$ to $T = 10$ days. All figures and the different properties are given at $T = 10$ days for the first layer of the six-layer model.

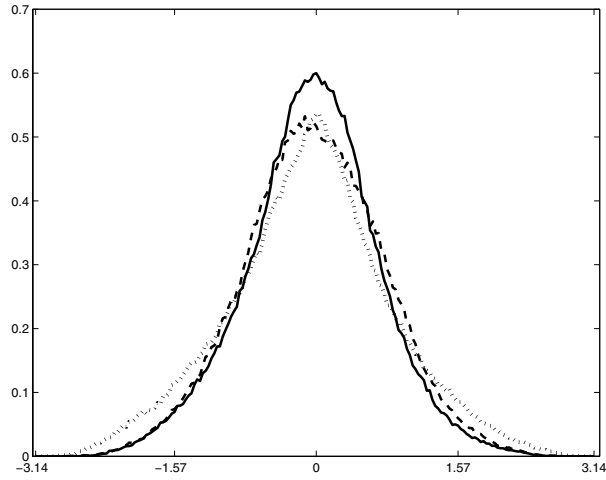


Figure 3. The probability density function at $T = 10$ days of $\zeta' - \zeta_{-}^{r'}$ (dashed line), of $\zeta' - \zeta_{-}^r$ (dotted line) and of $\zeta' - \zeta_{-}^{r_{ow}}$ (solid line) conditioned by $|r'| < 1$, $|r_{ow}| < 1$, $|r| < 1$ and $\delta > |\delta|_{\max}/10$. This statistic is obtained from an ensemble of 200 perturbations.

(a) *Alignment dynamics*

(i) *Regions of large δ .* Our aim is to discover if the analytical orientations found in section 2 emerge or not, and to identify the most representative orientation for the perturbation structure. Figure 3 represents the probability density function (PDF) of the three different angles $(\zeta' - \zeta_{-}^{r'})$, $(\zeta' - \zeta_{-}^r)$ and $(\zeta' - \zeta_{-}^{r_{ow}})$ calculated for 200 random perturbations conditioned by $|r'| < 1$, $|r_{ow}| < 1$, $|r| < 1$ and $\delta > |\delta|_{\max}/10$. A point to note is that we consider the intersection between regions where the three analytical orientations exist, i.e. where $|r'| < 1$, $|r_{ow}| < 1$, $|r| < 1$, in order to compare the three PDFs. For this threshold of large δ , there is a preferential orientation linked with the Okubo–Weiss criterion $\zeta_{-}^{r_{ow}}$ since the PDF of $(\zeta' - \zeta_{-}^{r_{ow}})$ has a stronger peak than the other two PDFs. In other words, in regions of large δ , \mathbf{E} and \mathbf{D} are statistically non-collinear and form a non-trivial angle determined by $\pi/2 + \zeta_{-}^{r_{ow}}$. The fact that the orientation $\zeta_{-}^{r_{ow}}$ is more probable than $\zeta_{-}^{r'}$ and ζ_{-}^r is an unexpected result, since we saw in section 2 that the most accurate criteria should take into account the rotation of the vector \mathbf{D} . As such criteria represented by the orientations $\zeta_{-}^{r'}$ and ζ_{-}^r are derived from two distinct approximations, it is unclear why the orientation $\zeta_{-}^{r_{ow}}$ included in the interval $[\zeta_{-}^{r'}, \zeta_{-}^r]$ ($r_{ow} \in [r', r]$) emerges. Even if the differences between $\zeta_{-}^{r_{ow}}$ and the other two orientations $\zeta_{-}^{r'}$ and ζ_{-}^r are not so large, these differences appear robust and are also found for other finite times (e.g. at $T = 20$ days) and for other spatial-scale perturbations. Despite the fact that other terms are involved in the dynamics of the numerical simulations (baroclinic stretching term and dissipation), the perturbation velocity vector aligns with an equilibrated orientation that can be analytically predicted from the combined action of the stretching mechanism by the basic-flow shear $\nabla \bar{\mathbf{u}}$ and by the pressure-gradient correction term.

Let us focus on the exponential kinetic-energy generation rate δ defined in section 2(a). The ensemble mean (represented by the symbols $\langle \rangle$) of the absolute exponential generation rate for the 200 Monte-Carlo realizations $\delta_{MC} \equiv \langle |\bar{\sigma} \sin \zeta'| \rangle$ is compared with analytical estimates of the instantaneous exponential generation rate of the perturbation kinetic energy. The influence of the angle ζ' on the spatial localization

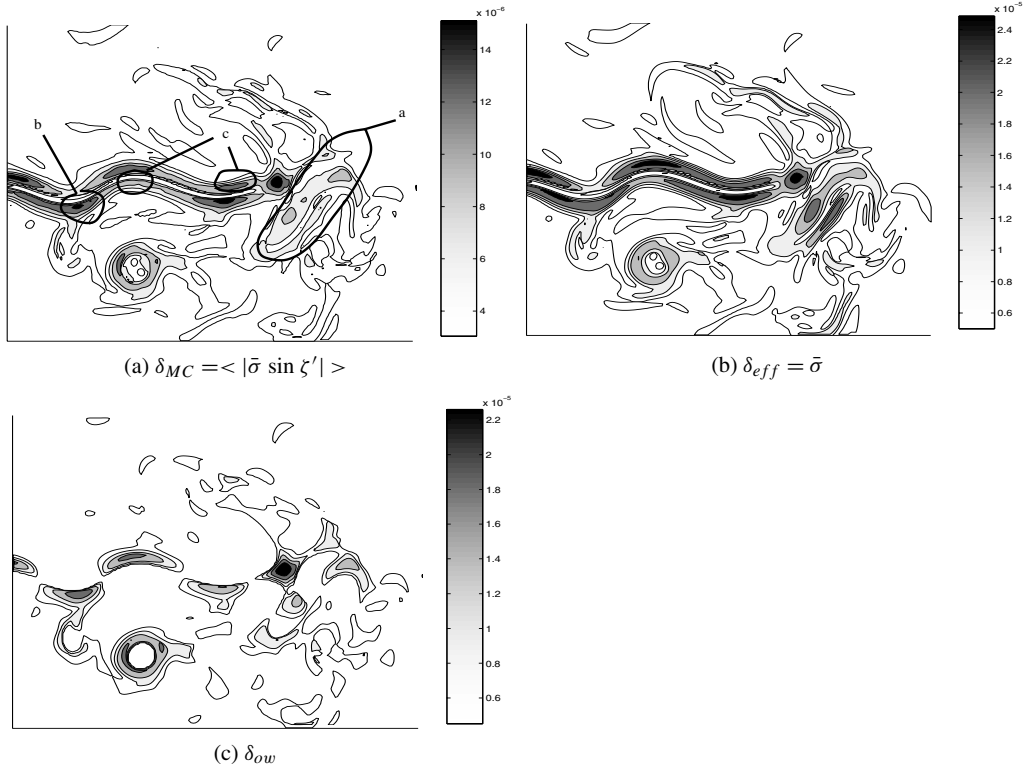


Figure 4. Spatial localization of exponential generation rates (s^{-1}) at $T = 10$ days inside area A; (a) the ensemble mean of the absolute exponential generation rate for 200 independent realizations, (b) the rate of strain $\delta_{eff} = \bar{\sigma}$, and (c) the estimated exponential generation rate δ_{ow} . Note that the grey scales are different for (a), (b) and (c). See text for a discussion of the labelled subdomains in (a).

of the Monte-Carlo exponential generation rate is noticeable in Fig. 4. If we look at the exit of the jet (subdomain ‘a’ in Fig. 4(a)), $\bar{\sigma}$ (Fig. 4(b)) presents two strong maxima which do not correlate with the Monte-Carlo generation rate (Fig. 4(a)) because $|\sin \zeta'|$ is close to zero in these regions. This behaviour of the Monte-Carlo generation rate in region ‘a’ is clearly reproduced by the estimated generation rate δ_{ow} (Fig. 4(c)). Regions such as subdomain ‘a’ are such that maxima of $\bar{\sigma}$ do not correspond to maxima of the generation rate because of strong vorticity values, which imply approximately that $\delta_{ow} = \sqrt{\bar{\sigma}^2 - \bar{\omega}^2} \simeq 0$. Other regions reveal good correlation of δ_{ow} with δ_{MC} , especially the subdomain ‘b’ located near the jet core, which exhibits a local maximum for the fields δ_{MC} and δ_{ow} but not for the rate of strain $\bar{\sigma}$. These two different subdomains illustrate the important role played by the orientation of the structure on the spatial localization of the kinetic-energy generation rate. The estimated exponential generation rate δ_{ow} is more representative of the Monte-Carlo exponential generation rate δ_{MC} than the rate of strain $\bar{\sigma}$. However, the analytical estimate, δ_{ow} , cannot apply within regions where $|r_{ow}| > 1$ which clearly exist along the jet axis; this is the case of subdomain ‘c’, for instance, where no special orientation can be diagnosed by our method. In such regions, there is no real eigenvalue, whereas the mean exponential generation rate is not too small (nor too large) and our approach does not provide a particular orientation.

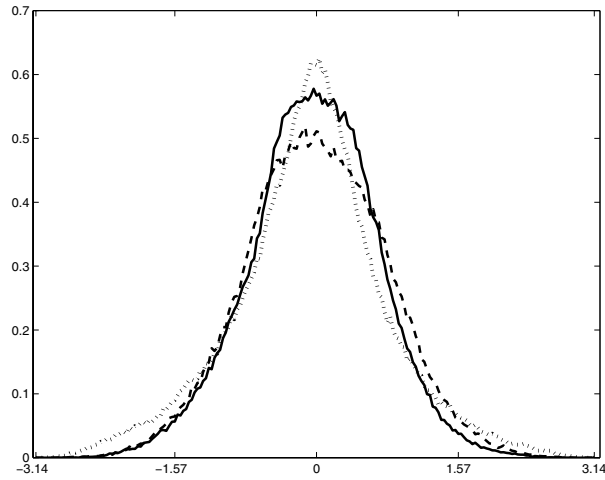


Figure 5. The probability density function at $T = 10$ days of $\zeta' - \zeta_-^{r'}$ (dashed line), of $\zeta' - \zeta_-^r$ (dotted line) and of $\zeta' - \zeta_-^{r_{ow}}$ (solid line) conditioned by $|r'| < 1$, $|r_{ow}| < 1$, $|r| < 1$ and $\mathbf{E} \cdot \mathbf{D} > |\mathbf{E} \cdot \mathbf{D}|_{\max}/200$. This statistic is obtained with an ensemble of 200 perturbations.

(ii) *Regions of large kinetic-energy extraction.* In Fig. 5, the same PDFs as in Fig. 3 are shown, but for regions characterized by large kinetic-energy extraction $\mathbf{E} \cdot \mathbf{D} = \delta|\mathbf{u}'|^2/2$, where the perturbation can extract the most kinetic energy. In these regions of large $\mathbf{E} \cdot \mathbf{D}$, the fixed point calculated with pressure $\zeta_-^{r'}$ is the most probable and performs slightly better than the eigenvector orientation $\zeta_-^{r_{ow}}$, and much better than the fixed point ζ_-^r computed without considering the pressure term. This result is robust to different types of random perturbation, and has also been found in doubly-periodic quasi-geostrophic flows (not shown here). In these regions, it is difficult to distinguish which of ζ_-^r and $\zeta_-^{r_{ow}}$ is the most representative because, on the one hand the PDF of $(\zeta' - \zeta_-^r)$ has a slightly higher peak around the abscissa 0 than the PDF of $(\zeta' - \zeta_-^{r_{ow}})$, but on the other hand regions where $|r_{ow}| < 1$ and $\mathbf{E} \cdot \mathbf{D} > |\mathbf{E} \cdot \mathbf{D}|_{\max}/200$ represents 59% of the regions determined by $\mathbf{E} \cdot \mathbf{D} > |\mathbf{E} \cdot \mathbf{D}|_{\max}/200$, whereas regions where $|r| < 1$ and $\mathbf{E} \cdot \mathbf{D} > |\mathbf{E} \cdot \mathbf{D}|_{\max}/200$ concern only 45%.

Figures 3 and 5 show PDFs in regions of positive extraction, i.e. in productive regions of kinetic energy ($\mathbf{E} \cdot \mathbf{D} > |\mathbf{E} \cdot \mathbf{D}|_{\max}/200$). But the joint PDF of the Monte-Carlo exponential generation rate with the analytical expression given by δ_{ow} (shown in Fig. 6) considers both productive and destructive regions ($|\mathbf{E} \cdot \mathbf{D}| > |\mathbf{E} \cdot \mathbf{D}|_{\max}/200$). The analytical growth rate δ_{ow} corresponds to a good approximation of the Monte-Carlo growth rate because a strong branch which involves most of the points is superposed to the bisector of the right quadrant. This strong branch corresponds to a production of kinetic energy for the random perturbations and a correlation of $+1$ with the analytically estimated growth rate δ_{ow} . However, another less visible branch is approximately superposed on the bisecting line of the left quadrant and is linked with a destruction of kinetic energy and a correlation of -1 with δ_{ow} . This destructive branch is connected with the destructive fixed point $\zeta_+^{r_{ow}}$. A similar diagram for the analytical generation rate δ_r shows the same properties. In the present ensemble with large-scale initial perturbations, productive regions are much more space filling than the destructive ones, and a clear alignment with ζ_-^r or $\zeta_-^{r_{ow}}$ is visible. The proportion between productive and destructive regions of kinetic energy depend on the spatial scales of random perturbations. The other cases examined revealed that destructive regions can be significantly important and that,

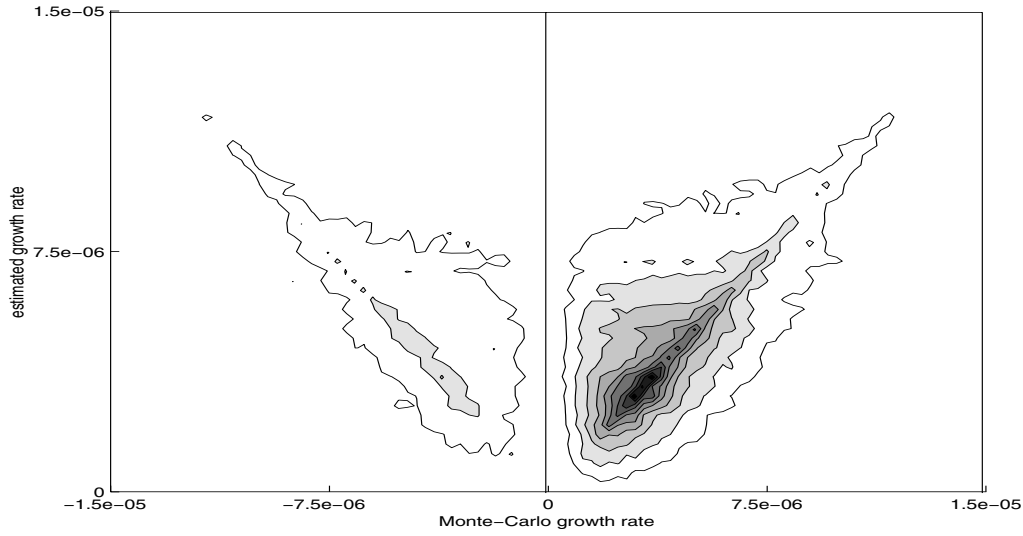


Figure 6. The joint probability density function at $T = 10$ days of the Monte-Carlo exponential generation rate with the estimate δ_{ow} conditioned by $|r_{ow}| < 1$ and $|\mathbf{E} \cdot \mathbf{D}| > |\mathbf{E} \cdot \mathbf{D}|_{\max}/200$.

within these regions, the angle ζ' is close to the destructive orientations ζ_+^r or ζ_{+ow}^r . A generic property seems to emerge; in regions of production a strong alignment with ζ_-^r or ζ_{-ow}^r occurs while in regions of destruction an alignment occurs with ζ_+^r or ζ_{+ow}^r .

To conclude with the PDF results, Figs. 3, 5 and 6 show that the two types of preferred orientation ($\zeta_{\pm}^{r_{ow}}$ and ζ_{\pm}^r) derived by taking into account the pressure gradient are the most probable orientations; it is clearly proven that the orientation $\zeta_{\pm}^{r'}$ derived without the pressure term is less relevant.

Let us now compare more quantitatively the different growth rates obtained by performing both a spatial and an ensemble average, denoted by $\langle\langle \rangle\rangle$, inside the kinetic energy production regions defined by $|r'| < 1$, $|r_{ow}| < 1$, $|r| < 1$ and $\mathbf{E} \cdot \mathbf{D} > |\mathbf{E} \cdot \mathbf{D}|_{\max}/200$. Such a threshold enables us to consider regions where fixed points exist and where perturbations extract energy from the reference flow.

$$\langle\langle \delta_{\text{eff}} \rangle\rangle = 1.1 \cdot 10^{-5} \text{ s}^{-1},$$

$$\langle\langle \delta_{r'} \rangle\rangle = 8.9 \cdot 10^{-6} \text{ s}^{-1},$$

$$\langle\langle \delta_{ow} \rangle\rangle = 8.5 \cdot 10^{-6} \text{ s}^{-1},$$

$$\langle\langle \delta_r \rangle\rangle = 6.1 \cdot 10^{-6} \text{ s}^{-1},$$

$$\langle\langle \delta_{\text{MC}} \rangle\rangle = 6.9 \cdot 10^{-6} \text{ s}^{-1}.$$

All the above values are obtained with large spatial-scale perturbations and can change if we choose another ensemble of perturbations. However, the generic property is that $\delta_{\text{eff}} > \delta_{r'} > \delta_{ow} > \delta_{\text{MC}} > \delta_r$. This comparison shows that $\delta_{r'}$ has a more efficient structure to extract energy than δ_{ow} , which itself is more efficient than δ_r . However, δ_{ow} and δ_r better represent the Monte-Carlo growth rate since they are closer to $\langle\langle \delta_{\text{MC}} \rangle\rangle$, as shown above. From a predictability point of view, the information provided by δ_{ow} and δ_r is more useful and more accurate than that of $\delta_{r'}$ or δ_{eff} for approximating the kinetic-energy error growth after a finite time. We remark also that δ_{ow} overestimates

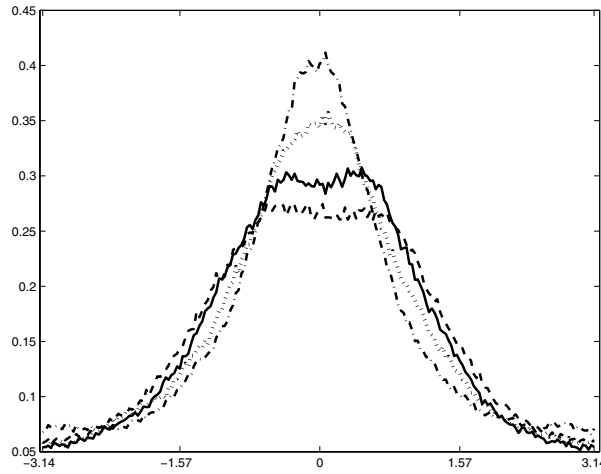


Figure 7. The probability density functions at $T = 10$ days of $\zeta' - \zeta'_0$ (dash-dotted line), $\zeta' - \zeta'^r$ (dashed line), $\zeta' - \zeta'^r$ (dotted line) and $\zeta' - \zeta'^{ow}$ (solid line), conditioned by $|r'| < 1$, $|r_{ow}| < 1$, $|r| < 1$ and $|u'| > |u'|_{\max}/10$.

the kinetic-energy error growth while δ_r slightly underestimates it. In the present case δ_r is closer to $\langle\delta_{MC}\rangle$ than δ_{ow} , but for other perturbations the reverse can occur.

(iii) *Regions of large kinetic energy.* In MC, the authors insisted on the fact that regions of energy extraction do not coincide spatially with regions of large energy because of the redistribution processes of the pressure work and the advection term. Which alignment is characteristic of large values of kinetic energy? To answer this question let us define the following angle

$$\zeta'_0 \equiv \begin{cases} 0 & \text{if } r_{ow} > 0 \\ -\pi & \text{if } r_{ow} < 0. \end{cases} \quad (29)$$

This angle is characterized by no extraction; indeed, if $\zeta' = \zeta'_0$, then the associated growth rate δ is equal to zero and the two vectors \mathbf{E} and \mathbf{D} are perpendicular. This angle has also the property of being continuous with the angle ζ'^{ow} of the eigenvector direction of $\nabla \bar{\mathbf{u}}$ for $r_{ow} = \pm 1$. The PDF of $(\zeta' - \zeta'_0)$ is compared with that of the three analytical orientations in Fig. 7 in regions of large kinetic energy. The most probable angle in these regions is clearly the angle ζ'_0 corresponding to no extraction. This result shows that regions where the kinetic energy is already redistributed are characterized by an equilibrium where no production and no destruction occurs, and where the two vectors \mathbf{E} and \mathbf{D} are perpendicular. The second better PDF concerns the fixed point with pressure ζ'^r ; this is logical because, among the three analytical orientations derived in section 2, it corresponds to the less efficient structure and, thus, defines an angle between \mathbf{E} and \mathbf{D} close to $\pi/2$. The spatial separation between regions of large extraction and regions of strong kinetic energy can be viewed now in terms of perturbation structure; regions of extraction are characterized by a non-trivial angle between \mathbf{E} and \mathbf{D} determined by either $\pi/2 + \zeta'^{ow}$ or $\pi/2 + \zeta'^r$, and regions of large kinetic energy exhibit no tilt against the shear and \mathbf{E} and \mathbf{D} are perpendicular. An interesting feature is that, for the tracer-gradient dynamics, such a distinction is not discernible in Fig. 5(a) of L99, and regions of strong PV gradient are also characterized by large growth rates of PV gradient.

(iv) *Check on the consistency of the parametrization of the ageostrophic pressure gradient.* One important conclusion from the analytical calculations of section 2 was

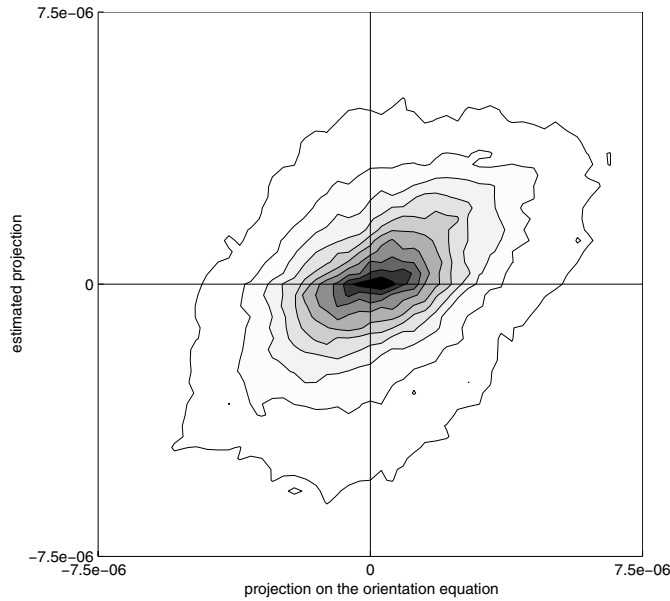


Figure 8. The joint probability density function at $T = 10$ days of the projection of the pressure gradient on the orientation equation $P_\theta(p'_1)$ with the analytical estimate $\bar{\sigma}(r_{ow} + \cos \zeta')$ conditioned by the same threshold as in Fig. 6.

that the ageostrophic pressure gradient plays a decisive role in favouring the eigenvector directions of $\nabla \bar{\mathbf{u}}$ and the orientations ζ_\pm^r . This influence of the ageostrophic term was deduced from an analytical approximation of the projection of the pressure gradient $P_\theta(p'_1)$ on the orientation equation (see (25)). Figure 8 is a joint PDF of $P_\theta(p'_1)$ with the analytical approximation $\bar{\sigma}(r_{ow} + \cos \zeta')$. Figure 8 does not take into account the β -term; the equivalent expression with the β -term is indicated in appendix B. The figure shows an ellipsoid centred around the point $(0, 0)$, the principal axis of which is close to the first bisecting line. The ratio between the major axis and the small axis is almost 1.5. This means that the analytical formula is significant, and permits us to capture the real pressure-gradient behaviour. Most of the points are localized around the point $(0, 0)$; the fact that the pressure-gradient projection is close to zero ($x = 0$) for the eigenvector directions ($y = 0$) is thus confirmed numerically. The analytical approximation of $P_\theta(p'_1)$, even if it is derived from a strong assumption, is thus significant and represents rather well the influence of the pressure gradient.

(v) *Alignment rationalization.* All previous results concerning the relative orientations of \mathbf{E} and \mathbf{D} are summarized by the sketch drawn in Fig. 9. The plot is obtained for a typical perturbation structure which is initially large scale. After ten days, the spatial structure of the perturbation moves with the meanders of the jet and has a typical spatial scale comparable with the meanders. The dynamical characteristics of the different regions can be inferred from the orientation of the perturbation streamlines relatively to the shear. Regions between lines ‘a’ and ‘d’ are productive regions; the perturbation can extract energy from the basic flow since the perturbation leans against the shear. Between lines ‘a’ and ‘c’, the perturbation structure is the most efficient, as \mathbf{E} and \mathbf{D} are close to collinearity; δ is large and the most probable orientation is $\zeta_-^{r_{ow}}$. Between lines ‘c’ and ‘d’, the structure is less efficient, but the kinetic energy is important (tight streamlines); this is a region of large extraction ($\mathbf{E} \cdot \mathbf{D} > 0$) where the most probable

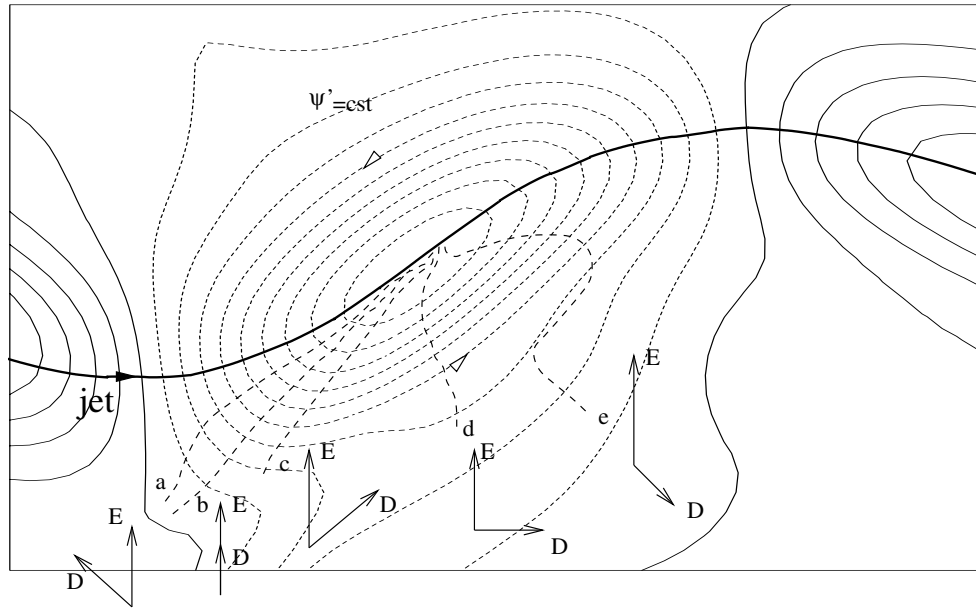


Figure 9. Sketch summarizing the different results of the alignment dynamics of a typical large spatial-scale perturbation around the jet at $T = 10$ days. The jet axis corresponds to the bold continuous line, perturbation stream-function isolines are the thin continuous and dashed lines. Isolines of $\pi/2 + \zeta'$ for this particular perturbation correspond to the bold dashed lines: $-\pi/4$ (line 'a'), 0 (line 'b'), $\pi/4$ (line 'c'), $\pi/2$ (line 'd'), and $3\pi/4$ (line 'e'). Note that, for simplicity, the direction of \mathbf{E} is arbitrarily plotted parallel to the y -axis everywhere. See text for further explanation.

orientations are $\zeta_{-}^{r_{ow}}$ and ζ_{-}^r . Line 'd' is the line where \mathbf{E} and \mathbf{D} are perpendicular and corresponds almost to a line of maximum kinetic energy. Regions lying between lines 'd' and 'e' are destructive, and the most probable structures are given by $\zeta_{+}^{r_{ow}}$ and ζ_{+}^r .

(b) Error fields

The following results present the spatial distribution of the error fields and their relation to the reference flow. An interesting result noticed by Snyder and Hamill (2003) for Lyapunov vectors, and Snyder *et al.* (2003) with a Monte-Carlo technique, is that the potential-vorticity error field (q') is localized in regions of large gradients of potential vorticity of the reference flow ($|\nabla \bar{q}|$). This strong correlation is also present in our case at $T = 10$ days (see Figs. 10(a) and (b)). This property was first proved analytically by Thompson (1986) for homogeneous, isotropic initial-error assumptions, and systematic numerical experiments in quasi-geostrophic flows performed by the above authors suggest that this is a generic property. Even if a transient initial phase can occur for layers in the domain interior in which the PV error field is not yet stabilized, Snyder *et al.* (2003) systematically found that after two days (in an atmospheric quasi-geostrophic model) a concentration of PV error in regions of large PV gradient of the reference flow. In our case, at $T = 10$ days all the layers present a strong correlation between the root-mean-square of the PV error field calculated with 200 perturbations (Fig. 10(a)) and the PV gradient of the control flow (Fig. 10(b)). The same feature can be found with the relative-vorticity variable, as seen when comparing Fig. 10(c) with Fig. 10(d). Indeed, relative-vorticity errors (Fig. 10(c)) are localized in regions where the relative-vorticity gradient of the reference flow (Fig. 10(d)) is large. For example,

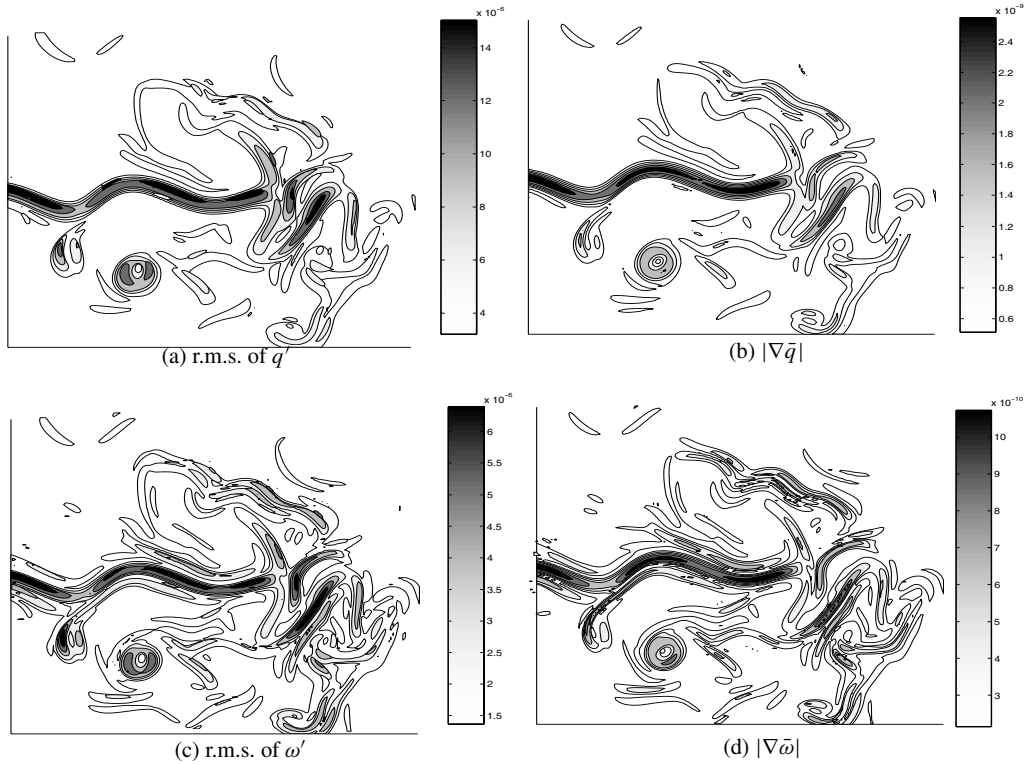


Figure 10. Comparison between the spatial structures of the perturbations and those of the reference flow: (a) the root-mean-square of the potential-vorticity (PV) error field (s^{-1}) (convergence to within 1% obtained with 200 perturbations), (b) the magnitude of the horizontal PV gradient of the reference flow ($\text{m}^{-1}\text{s}^{-1}$), (c) the root-mean-square of the relative-vorticity error field (s^{-1}), and (d) the magnitude of the horizontal relative-vorticity gradient of the reference flow ($\text{m}^{-1}\text{s}^{-1}$).

fields related to PV (Figs. 10(a) and (b)) only present one large maximum along the jet, whereas those related to relative vorticity (Figs. 10(c) and (d)) have three bands of maxima along the jet, with the largest one near the jet core. Moreover, small-scale structures of ω' in the region north of the jet axis are well represented by $|\nabla \bar{\omega}|$, but not at all by $|\nabla \bar{q}|$. This suggests that, for a given scalar variable s , its error growth s' is localized in regions of strong $|\nabla \bar{s}|$, and the essential ingredient seems to be the linearization of $Ds/Dt = 0$ ($\bar{D}s'/Dt = -\mathbf{u}' \cdot \nabla \bar{s}$).

But what is occurring for the kinetic-energy error growth? By analogy with scalar results and the linearized velocity equation (2), a comparison between the root-mean-square of the kinetic-energy error field (u') and the velocity-gradient tensor $\nabla \bar{\mathbf{u}}$ is tested in Fig. 11. The u' maxima (Fig. 11(a)) are localized in regions where the norm of $\nabla \bar{\mathbf{u}}$ is large (Fig. 11(b)) (its norm is defined as $\sqrt{\bar{\sigma}^2 + \bar{\omega}^2}$), and is not always in regions of strong vorticity (Fig. 11(c)) or of strong rate of strain (Fig. 11(d)). For instance, the kinetic-energy error field (Fig. 11(a)) presents a strong maximum at the jet exit that is also seen in $\bar{\sigma}$ (Fig. 11(d)) but not in $\bar{\omega}$ (Fig. 11(c)). By contrast, for the isolated eddy located in the lower left part of the figure, the kinetic error field (which is very strong inside the eddy core) is well correlated with $\bar{\omega}$ but not at all with $\bar{\sigma}$. The correct field, which is well correlated with the kinetic error field, is thus $\sqrt{\bar{\sigma}^2 + \bar{\omega}^2}$. This last result concerning kinetic-energy error localization is another property showing how the tensor

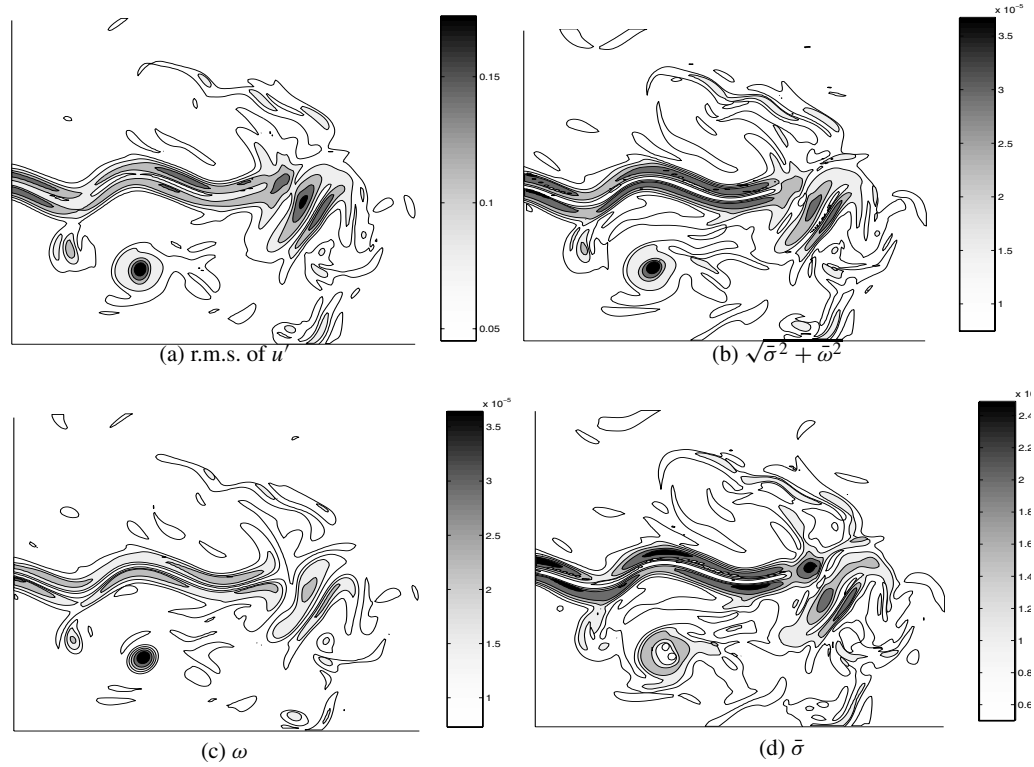


Figure 11. Comparison between the spatial structures of the kinetic-energy error field u' and the spatial properties of the basic-state velocity-gradient tensor $\nabla \mathbf{u}$: (a) the root-mean-square of the kinetic-energy error field (m s^{-1}), (b) the norm of $\nabla \mathbf{u}$: $\sqrt{\sigma^2 + \omega^2}$ (s^{-1}), (c) the relative vorticity $\bar{\omega}$ (s^{-1}), and (d) the rate of strain $\bar{\sigma}$ (s^{-1}).

$\nabla \mathbf{u}$ influences the perturbation velocity-field behaviour. Another important remark is that regions of large perturbation kinetic energy (Fig. 11(a)) are well separated from regions where exponential generation rates are strongest (Fig. 4(a)) as already noted in section 3(a). For example, along the jet, the largest growth rates are localized around the top of the meanders (region ‘b’ in Fig. 4(a)) whereas the kinetic energy error field has maxima in regions where the curvature of the jet is the smallest. This spatial separation is also clear for the isolated eddy; the perturbation kinetic energy is large in the centre of the eddy whereas the exponential generation rates are localized around it (see Fig. 4(a)).

4. CONCLUSION

In this paper, we have focused on the generation term of the perturbation kinetic energy to get some information on how the error due to uncertain initial conditions in the model state can grow. As shown by MC, the generation term is the scalar product between two vectors \mathbf{E} and \mathbf{D} , and is thus strongly dependent on the angle between \mathbf{E} and \mathbf{D} ($\pi/2 + \zeta'$ in our notations). We have shown that the preferred values of this angle ζ' can be found by analysing the linearized momentum equations in their Lagrangian form and, more precisely, the orientation equations for the perturbation velocity that are inferred. A simple parametrization of the ageostrophic pressure term has been verified to be not too far from the real ageostrophic pressure-gradient behaviour. The preferred orientations that are predicted analytically are composed of two couples ($\zeta_{-}^{\text{row}}, \zeta_{+}^{\text{row}}$)

and (ζ_-^r, ζ_+^r) . The couple $(\zeta_-^{r_{ow}}, \zeta_+^{r_{ow}})$ corresponds to the orientation of the eigenvectors of $\nabla \bar{\mathbf{u}}$, the couple (ζ_-^r, ζ_+^r) corresponds to fixed points of the orientation equation. It has been shown numerically with a Monte-Carlo technique that the perturbation angle ζ' is close to $\zeta_-^{r_{ow}}$ in regions of large exponential generation rate. In regions of large extraction, $\zeta_-^{r_{ow}}$ or ζ_-^r are the two most probable values for ζ' . Finally, in regions where extraction occurs, the two significant orientations are those derived from the best approximate orientation equation which takes into account the ageostrophic pressure gradient. This unexpected result comes from the fact that the orientation associated with the eigenvector of $\nabla \bar{\mathbf{u}}$ is globally more relevant than the orientation that takes into account the rotation of \mathbf{D} . This result is still unclear to us, but it should be kept in mind that our parametrization of the pressure gradient is rather coarse.

We have observed that the destructive orientations given by $\zeta' = \zeta_+^{r_{ow}}$ and by $\zeta' = \zeta_+^r$ are the preferred orientations in the energy destructive regions, which for other types of random ensembles can be almost as important as the productive regions. The generic property is the alignment with $\zeta_-^{r_{ow}}$ or ζ_-^r in productive regions and with $\zeta_+^{r_{ow}}$ or ζ_+^r in destructive regions, while the proportion between productive and destructive regions depends on the perturbation spatial scales and on the finite time length.

Concerning the alignment dynamics in regions of strong kinetic energy, we have found that \mathbf{E} and \mathbf{D} are perpendicular, and that these regions are characterized by no extraction.

These results on alignment dynamics provide an analytical tool for estimating the spatial localization of the exponential generation rate and its spatial average. The spatial average estimations $\langle \delta_{ow} \rangle$ or $\langle \delta_r \rangle$ are useful global diagnostics for quantifying the kinetic-energy exponential generation rate, and for providing a better evaluation of the predictability time of a given flow than the average rate of strain. The estimations of the local exponential generation rate could be used to locate the specific regions where unstable structures are the most probable; such regions would be characterized by both a strong rate of strain and a weak vorticity in the reference flow.

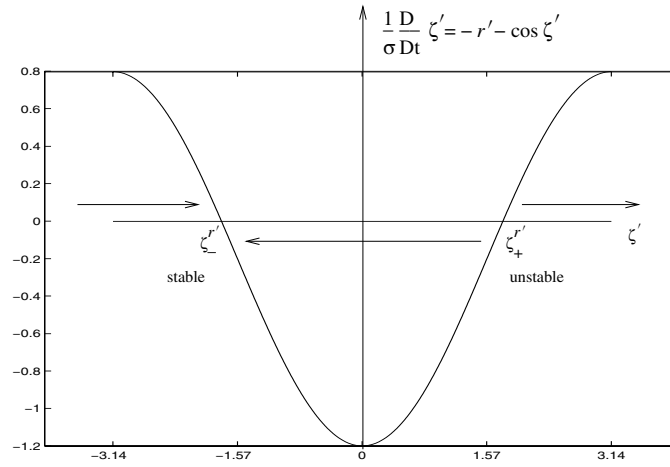
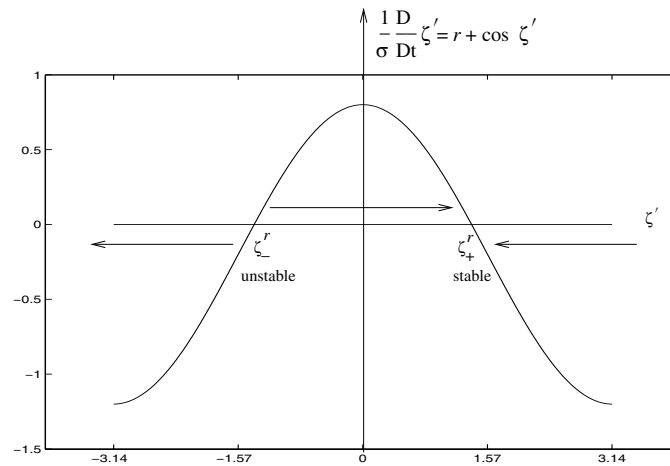
An intrinsic limitation of our Lagrangian approach is that we cannot systematically characterize the two main redistribution terms—the advection of the energy by the basic flow and the ageostrophic pressure work—and we cannot explain why all the maxima of the kinetic-energy error field are concentrated in regions where the norm of $\nabla \bar{\mathbf{u}}$ is large. We have found numerically, however, that this spatial distribution of the kinetic-energy errors is mainly governed by the generation-rate term which depends strongly on $\nabla \bar{\mathbf{u}}$.

The ageostrophic pressure gradient is also a function of the basic-state strain field (see (18)), and thus participates to the spatial correspondences between $|\mathbf{u}'|$ and the norm of $\nabla \bar{\mathbf{u}}$. Furthermore, accurate analytical analyses should be attempted to clarify the ageostrophic pressure-gradient role.

Finally, we want to emphasize that our analytical diagnostics, which have been obtained with a single simulation, agree with the statistics obtained by the Monte-Carlo approach that have required 200 simulations. Such an analytical approach is thus much less computationally intensive than an ensemble-prediction method.

ACKNOWLEDGEMENTS

We would like to thank Joe Tribbia for valuable comments on this manuscript. The calculations reported here were done on the NEC SX-5 computer of the Institut du Développement et des Ressources en Informatique Scientifique (IDRIS), Orsay, France (project no. 021217), and during this work G. Rivière was supported by a Délégation Général pour l'Armement fellowship.

Figure A.1. Stability diagram of (15b) for $|r'| < 1$.Figure A.2. Stability diagram of (27) for $|r| < 1$.

APPENDIX A

Stability analysis

Figure A.1 shows the stability diagram of (15b); the productive fixed point $\zeta_-^{r'}$ is stable, whereas the destructive fixed point $\zeta_+^{r'}$ is unstable. Likewise $\zeta_-^{r_{ow}}$ is stable whereas $\zeta_+^{r_{ow}}$ is unstable.

Figure A.2 corresponds to the stability analysis of the complete orientation equation (27); the productive fixed point ζ_-^r is unstable whereas the destructive one is stable. Similar results can be obtained for the eigenvector directions when we consider the complete equation (26); the productive structure is unstable whereas the destructive one is stable. All these differences between the orientation equations with the pressure term and those without it stem from the fact that the projection of the pressure gradient on the orientation equation is twice the opposite of the projection of $-\nabla \mathbf{u} \cdot \mathbf{u}'$.

APPENDIX B

Influence of the β -effect on the orientation equation

In presence of β , Eq. (2) has the following form

$$\frac{\overline{\mathbf{D}\mathbf{u}}'}{Dt} = -\nabla\overline{\mathbf{u}} \cdot \mathbf{u}' - \nabla p'_1 + \beta y \nabla \psi', \quad (\text{B.1})$$

which can also be written as

$$\frac{\overline{\mathbf{D}\mathbf{u}}'}{Dt} = -\nabla\overline{\mathbf{u}} \cdot \mathbf{u}' - \nabla\widehat{p}'_1 - \beta\psi'\mathbf{j}, \quad (\text{B.2})$$

where $\widehat{p}'_1 \equiv p'_1 - \beta y \psi'$ (same definition as in (2.3) of Hua *et al.* (1998)) and \mathbf{j} is the unit vector in the meridional direction. By taking the divergence of (B.2), we obtain

$$\Delta\widehat{p}'_1 = 2\{J(\overline{\mathbf{u}}, v') + J(u', \overline{v})\} + \beta u', \quad (\text{B.3})$$

and then, by inverting the Laplacian operator and applying the gradient operator,

$$-\nabla\widehat{p}'_1 - \beta\psi'\mathbf{j} = -\nabla[\Delta^{-1}\{2J(\overline{\mathbf{u}}, v') + 2J(u', \overline{v})\}] - \nabla\{\Delta^{-1}(\beta u')\} - \beta\psi'\mathbf{j}. \quad (\text{B.4})$$

The first term on the right-hand side is analysed in section 2(c), but the sum of the two other terms involves the β -term. Let us now consider the following vector $-\nabla(\Delta^{-1}(\beta u')) - \beta\psi'\mathbf{j}$ and its projection on the orientation equation. If we consider the monochromatic perturbation introduced in (19), we have $\beta u' = A\beta l \sin(kx + ly)$ and $-\beta\psi'\mathbf{j} = -A\beta \cos(kx + ly)\mathbf{j}$. By inverting the Laplacian for the first term $\Delta^{-1}(\beta u') = -A\beta l \sin(kx + ly)/(k^2 + l^2)$, and then by applying the gradient operator, $-\nabla\{\Delta^{-1}(\beta u')\} = A\beta l \cos(kx + ly)\mathbf{k}/(k^2 + l^2)$. The vector that involves β , $-\nabla\{\Delta^{-1}(\beta u')\} - \beta\psi'\mathbf{j}$, is generally non-zero, but let us look at its projection on $\mathbf{e}'_{\perp} = \pm(k, l)/\sqrt{k^2 + l^2}$. As

$$-\nabla\{\Delta^{-1}(\beta u')\} \cdot \mathbf{e}'_{\perp} = \pm \frac{-A\beta l}{\sqrt{k^2 + l^2}} \cos(kx + ly)$$

and

$$-\beta\psi'\mathbf{j} \cdot \mathbf{e}'_{\perp} = \pm \frac{A\beta l}{\sqrt{k^2 + l^2}} \cos(kx + ly),$$

we thus obtain $[-\nabla\{\Delta^{-1}(\beta u')\} - \beta\psi'\mathbf{j}] \cdot \mathbf{e}'_{\perp} = 0$, which means that for a monochromatic perturbation the β -term has no effect on the orientation equation.

This analytical estimate shows that taking into account the β -term does not change our main conclusion; the entire ageostrophic vector including the pressure and the β terms, $(-\nabla\widehat{p}'_1 - \beta\psi'\mathbf{j})$, is zero for the eigenvector directions of $\nabla\overline{\mathbf{u}}$.

APPENDIX C

The quasi-geostrophic ocean model

The numerical code is an extension of the basic two-layer box ocean model by Holland (1978), and a detailed description can be found in papers by Schmitz and Holland (1986) and Barnier *et al.* (1991). The physical variables are the stream function ψ_k in the layer k ($k = 1, 6$), the Coriolis parameter $f = f_0 + \beta y$, the steady sinusoidal wind stress τ at the ocean surface, the layer thickness H_k , the reduced gravity

$g'_{k+\frac{1}{2}}$ between layers k and $k+1$, the biharmonic frictional coefficient A_4 and the bottom frictional coefficient R . The quasi-geostrophic equations of motion for potential vorticity q_k

$$q_k = \nabla^2 \psi_k + f + \frac{f_0^2}{H_k} \left\{ \frac{1}{g'_{k-\frac{1}{2}}} (\psi_{k-1} - \psi_k) - \frac{1}{g'_{k+\frac{1}{2}}} (\psi_k - \psi_{k+1}) \right\}, \quad (\text{C.1})$$

is given by

$$\frac{Dq_k}{Dt} = -A_4 \nabla^6 \psi_k + \delta_{k,1} \frac{\text{curl } \tau}{H_1} - \delta_{k,6} R \nabla^2 \psi_n. \quad (\text{C.2})$$

The vertical boundary conditions correspond to rigid-lid conditions $w = 0$ at $z = 0$ and $z = H$, and the horizontal ones are determined by the free-slip conditions $\nabla^2 \psi_k = 0$ on all horizontal boundaries. The auxiliary conditions $\int \int (\psi_k - \psi_{k+1}) dx dy = 0$ for each layer $k \in [1, 5]$ are used for model consistency. Equation (C.2) is integrated using finite differences on a rectangular basin with horizontal dimensions $L_x = 3600$ km and $L_y = 3200$ km. The horizontal grid resolution is 10 km, and the different depths of the different layers are $H_1 = 300$ m, $H_2 = 350$ m, $H_3 = 400$ m, $H_4 = 500$ m, $H_5 = 1350$ m and $H_6 = 2100$ m. The steady wind stress is given by $\tau_0 = 0.6 \cdot 10^{-4} \text{ m}^2 \text{s}^{-2}$, the biharmonic coefficient by $A_4 = 1.5 \cdot 10^{-10} \text{ m}^4 \text{s}^{-1}$ and the bottom friction coefficient by $R = 10^{-7} \text{ s}^{-1}$.

APPENDIX D

The Monte-Carlo method

In this section, the initialization method of this ensemble is presented. All wave numbers are not excited in the same manner. In order to have physically relevant perturbations, we want the kinetic energy of the perturbation field to correspond to a k^{-3} spectrum. If a white noise is applied at each grid point for the perturbation horizontal PV gradient (in two dimensions a white noise corresponds to a k^{+1} spectrum), the spectrum of the perturbation PV q' is k^{-1} , and thus the kinetic energy has a k^{-3} spectrum. The horizontal PV-gradient perturbation is initialized as

$$\nabla q' = \begin{pmatrix} \epsilon_1 \\ \epsilon_2 \end{pmatrix}, \quad (\text{D.1})$$

where ϵ_1, ϵ_2 are random numbers selected uniformly on the interval $[-1, 1]$ (white noise). By applying the divergence on $\nabla q'$ and then a three-dimensional Poisson solver, the perturbation potential vorticity q' has indeed a k^{-1} spectrum and the kinetic energy a k^{-3} spectrum for most of the wave numbers. Such a spectrum is physically relevant and permits us to obtain a mean error field that converges for an ensemble of 200 realizations.

REFERENCES

- | | | |
|---|------|---|
| Barnier, B., Hua, B. L. and Leprovost, C. | 1991 | On the catalytic role of high baroclinic modes in eddy-driven large-scale circulations. <i>J. Phys. Oceanogr.</i> , 21 , 976–997 |
| Cai, M. and Mak, M. | 1990 | On the basic dynamics of regional cyclogenesis. <i>J. Atmos. Sci.</i> , 47 , 1417–1442 |
| Frederiksen, J. S. | 1983 | Disturbances and eddy fluxes in northern hemisphere flows: Instability of three-dimensional January and July flows. <i>J. Atmos. Sci.</i> , 40 , 836–855 |

- Holland, W. R. 1978 The role of mesoscale eddies in the general circulation of the ocean: numerical experiment using a wind-driven quasi-geostrophic model. *J. Phys. Oceanogr.*, **8**, 363–392
- Hoskins, B. J., James, I. N. and White, G. H. 1983 The shape, propagation and mean-flow interaction of large-scale weather systems. *J. Atmos. Sci.*, **40**, 1595–1612
- Hua, B. L., McWilliams, J. C. and Klein, P. 1998 Lagrangian accelerations in geostrophic turbulence. *J. Fluid Mech.*, **366**, 87–108
- Kucharski, F. and Thorpe, A. J. 2001 The influence of transient upper-level barotropic growth on the development of baroclinic waves. *Q. J. R. Meteorol. Soc.*, **127**, 835–844
- Lapeyre, G., Klein, P. and Hua, B. L. 1999 Does the tracer gradient vector align with the strain eigenvectors in 2D turbulence. *Phys. Fluids A*, **11**, 3729–3737
- Mak, M. and Cai, M. 1989 Local barotropic instability. *J. Atmos. Sci.*, **46**, 3289–3311
- Okubo, A. 1970 Horizontal dispersion of floatable particles in the vicinity of velocity singularities such as convergences. *Deep-Sea Res.*, **17**, 445–454
- Pierrehumbert, R. T. 1984 Local and global baroclinic instability of zonally varying flow. *J. Atmos. Sci.*, **41**, 2141–2162
- Schmitz, W. J. and Holland, W. R. 1986 Observed and modeled mesoscale variability near the Gulf Stream and Kuroshio Extension. *J. Geophys. Res.*, **91**, 9624–9638
- Simmons, A. J., Wallace, J. M. and Branstator, G. W. 1983 Barotropic wave propagation and instability, and the atmospheric teleconnection patterns. *J. Atmos. Sci.*, **40**, 1363–1392
- Snyder, C. and Hamill, T. M. 2003 Leading Lyapunov vectors of a turbulent baroclinic jet in a quasi-geostrophic model. *J. Atmos. Sci.*, **60**, 683–688
- Snyder, C., Hamill, T. M. and Trier, S. B. 2003 Linear evolution of error covariances in a quasi-geostrophic model. *Mon. Weather Rev.*, **131**, 189–205
- Straub, D. N. 2003 Instability of 2D flows to hydrostatic 3D perturbations. *J. Atmos. Sci.*, **60**, 79–102
- Thompson, P. D. 1986 A simple approximate method of stochastic-dynamic prediction for small initial errors and short range. *Mon. Weather Rev.*, **114**, 1709–1715
- Weiss, J. 1991 The dynamics of enstrophy transfer in two-dimensional turbulence. *Physica D*, **48**, 273–294